Systematic Pore Characterization of Sub-Bituminous Coal from Sohagpur Coalfield, Central India Using Gas Adsorption Coupled with X-ray Scattering and High-Resolution Imaging

Bhapkar, Pranay Vilas; Pradhan, Sarada Prasad; Chandra, Debanjan; Hazra, Bodhisatwa; Vishal, Vikram

Important note
To cite this publication, please use the final published version (if applicable).
Please check the document version above.

Systematic Pore Characterization of Sub-Bituminous Coal from Sohagpur Coalfield, Central India Using Gas Adsorption Coupled with X-ray Scattering and High-Resolution Imaging

Pranay Vilas Bhapkar, Sarada Prasad Pradhan,* Debanjan Chandra, Bodhisatwa Hazra, and Vikram Vishal

Read Online

ACCESS | Metrics & More | Article Recommendations | SI Supporting Information

ABSTRACT: Pore characterization helps to estimate the coalbed methane recovery and carbon storage potential of the reservoir. Earlier research on the characteristics of coal pores has shown that coal has high hydrocarbon storage potential in the adsorbed state, but few studies have shown the influence of chemical heterogeneities and depth on the adsorption potential of the coal. With the objective of studying the effect of chemical variation, depth, and surface roughness on gas adsorption potential, this study combines coal composition analysis and adsorption-based pore characterization of coal and shale samples coupled with high-resolution imaging and X-ray scattering measurements. Variation in pore features is correlated with varying depth and composition. A decrease in the mesopore volume and surface area is observed with an increase in the depth and total organic content and inverse behavior is observed for micropores. Scanning electron microscopy images depict the change in the pore shape from semi-spherical OM pores to elongated pores with depth, and samples with high mineral content show a dominance of inter- and intraparticle pores. Fractal dimension values estimated from SAXS are notably higher than N_2-LPGA-derived values (i.e.,—$D_S > D_N$) due to the incorporation of inaccessible pores, which reflects an increase of up to 62% in SAXS estimated mesopore volume and surface area. This study will provide a better approach to understand the impact of composition, depth, and surface roughness over the gas storage potential in coal reservoirs.
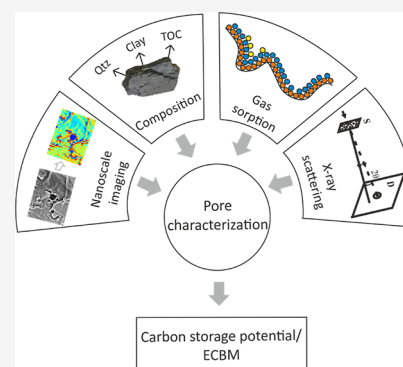
1. INTRODUCTION

Coalbed methane (CBM), an unconventional natural resource, is viewed as a potential option for boosting the global energy supply. In 2016, the global CBM market was valued at $9089 million and is anticipated to grow up to $17,956 million by 2023.[1] CBM is currently being looked at as a potential replacement for expanding India's energy supply. Under the Special round of CBM bidding 2021, the Government of India offered 15 CBM blocks in Madhya Pradesh, Jharkhand, Maharashtra, and Odisha. CBM production of 5 years until February 2020 is 2999.77 MMSCM from Jharkhand, West Bengal, and Madhya Pradesh and is expected to grow with the allocation of new CBM blocks. The exploration of CBM is greatly facilitated by the Indian coalfields.[2,3]

Coal and shale reservoirs are the proven potential sites for storing CO_2, which helps reduce the carbon concentration in the atmosphere and also enhances CBM recovery. For systematic storage of CO_2 and CH_4 recovery, it is essential to estimate the porosity and pore characteristics of the reservoir. In contrast to conventional reservoir rocks, coal consists of a highly complex pore system due to its widely distributed porosity. Primary gas storage sites are micro- and mesopores which are in the range of 1−50 nm and hence requires a nanoscale pore resolving instrument facility. A thorough study is required for establishing a relationship of total organic content (TOC), mineral matter, depth, and surface roughness with the gas storage potential to investigate the ECBM prospectives.

Previous studies have demonstrated the complex porosity system in coal. It is primarily influenced by coal rank, depth, organic matter, mineral composition, moisture, and reservoir temperature—pressure conditions.[4−10] The coal system possesses two different kinds of porosity: primary porosity, which is composed of meso- and micropores associated to the coal matrix, and secondary porosity, which is composed of fractures and cleats.[10−12] Pores are classified into three types based on size: (a) micropore- with a diameter < 2 nm, (b) mesopore- with a diameter between 2 and 50 nm, and (c) macropore with a diameter > 50 nm (IUPAC classification). Other pore
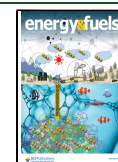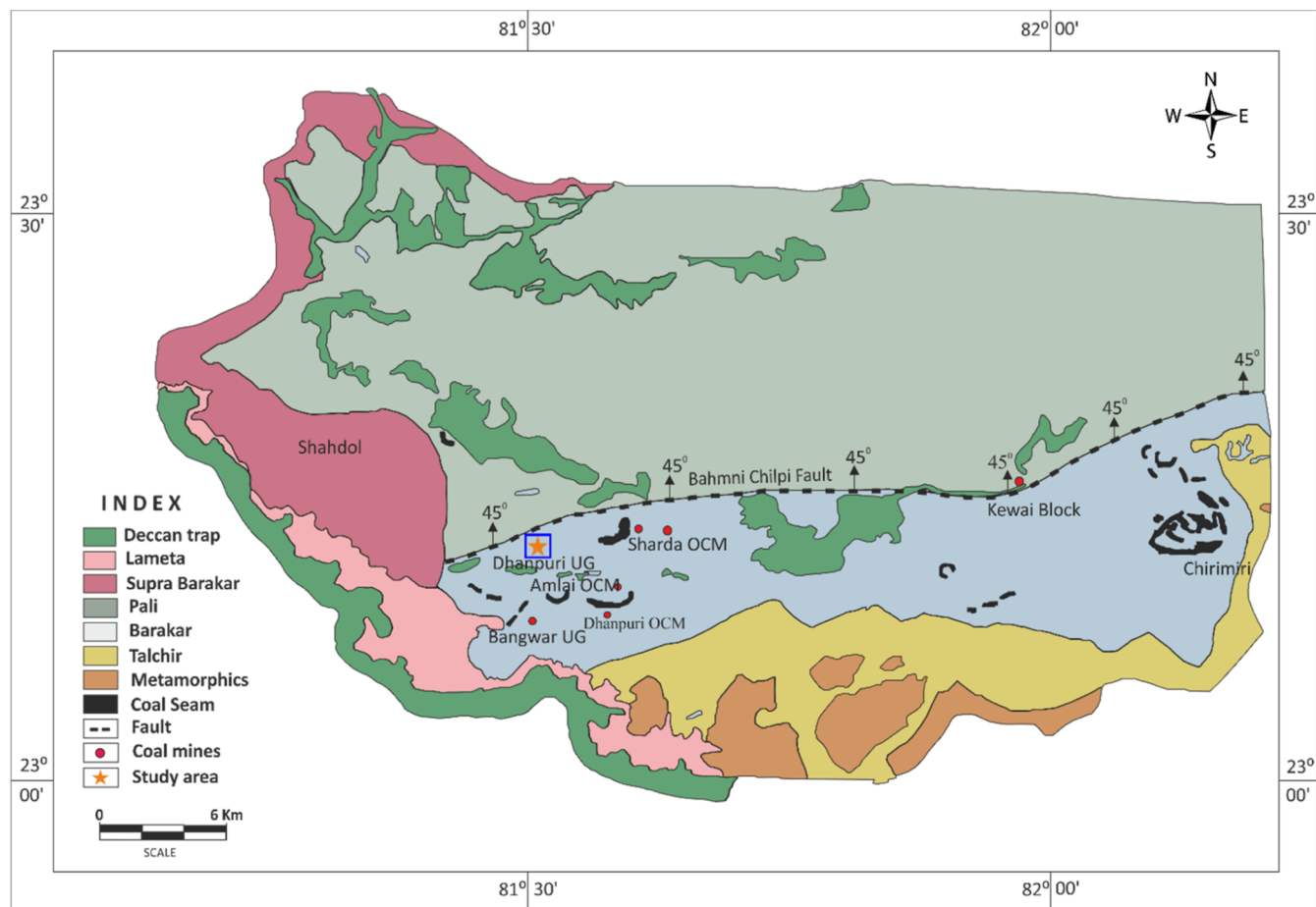
Figure 1. Geological map of Sohagpur coalfield, Madhya Pradesh with coalmine locations marked in red color. Reproduced with permission from Jasper et al.[34] Copyright 2016 John Wiley and Sons.

categorization techniques were published by Mays,[13] but they were not well received for coal reservoirs.

Micro- and mesopores are of primary interest in the pore characterization of coal, as these pores mainly hold the gas in the adsorbed state. In recent times, advanced instrumentation facilities have provided detailed insights into the nanoscale pores. High-resolution imaging, i.e., scanning electron microscopy (SEM), plays a vital role in the both qualitative and quantitative characterizations of structural characteristics and pore morphology.[14−17] Intrusive methods like low-pressure gas adsorption (LPGA) provide the quantitative characterization of gas accessible pore systems including surface area, pore volume, and pore size distribution (PSD).[17−21] Also, indirect methods like small angle X-ray scattering (SAXS) can provide pore attributes for both accessible and inaccessible pores.[22−24] Numerous investigations revealed divergent capacities of different types of organic content to produce hydrocarbons. Based on hydrogen index (HI) and oxygen index (OI) produced from Rock-Eval pyrolysis, kerogens in hydrocarbon source rocks can be roughly divided into four basic categories,[25,26] which indicates the potential of the source rock.

This study represents micro- and mesopore characteristics of coal samples from a prospective CBM field in India as well as their chemical composition using Rock Eval pyrolysis and powdered X-ray diffraction (XRD). Pore attributes are studied using LPGA, SAXS, and field emission gun-SEM (FEG-SEM). TOC, mineralogical composition, and depth are found to be

the significant parameters controlling pore characteristics. To assess the range of variance, variation in pore features was compared to the pore characteristics discovered from gas adsorption analysis of the coal and shale samples. Increasing depth and anisotropy in the samples due to TOC and mineral matter are estimated and their influence on adsorption potential is studied.

2. SAMPLES AND METHODOLOGY

2.1. Sampling. Five samples are selected for studying the chemical composition variation and pore characteristics based on the depth interval. Samples used for experimental work have a depth of 220, 397, 506, 723, and 848 m, respectively. Samples are labeled by using location as the prefix- "SGP" for Sohagpur and depth as a suffix; e.g., a sample recovered from a depth of 723 m is labeled as SGP-723. Furthermore, the sample preparation is split into two parts; the first part is used for obtaining flat flakes of ∼1 mm thickness for FEG-SEM imaging. The other portion is powdered using an agate mortar-pestle and sieved with 75 μm sieve. The finer portion passed through 75 μm sieve is used for chemical analysis and pore characterization (LPGA, XRD, Rock-Eval, and SAXS).

2.2. Geology of the Area. Sohagpur Coalfield is one of the significant central Indian coalfield spread across the Shahdol, Anuppur, and Umaria districts of Madhya Pradesh, also, eastern part of coalfield extends in Chhattisgarh.[27] This coalfield belongs to South Rewa Gondwana Basin with an estimated coal reserve of 4064 Mt and is spread out across an

area of around 3100 km² (1200 square miles).[28] A general trend of Gondwana sedimentary rocks in the area is in WNW-ESE to E-W, dipping 5° toward the north.[29] The coal deposits are 0−1200 m below the surface. The coalfield is divided into north and south blocks by E-W running the Bahmni-Chilpa fault (Figure 1).[30] Samples were recovered from the Dhanpuri UG (Figure 1) coal mine of Sohagpur coalfield, Madhya Pradesh, India, from a depth range of 220−848 m. Recovered samples are of the Barakar, Raniganj, and Lower Pali Formation of Late Permian to Early Triassic age. Samples were recovered in the form of cores from the drilling sites.

With ownership of 1000 km² in the east and west blocks of the Sohagpur coalfield, Reliance Industries Limited has made clear that there are large CBM resources present, the west block in particular has more CBM potential than the east block.[31] The government of India offered 5 CBM blocks in a special round of CBM-bid in 2021 to Madhya Pradesh, which is the maximum number of blocks compared to all other states. Barakar Formation with large reserves of bituminous and sub-bituminous coal deposits have low permeability and porosity but have potential CBM reserves in an adsorbed state.[32] The detailed geological succession of the Sohagpur coalfield is mentioned in Table 1.

Table 1. Detailed Stratigraphic Succession of Sohagpur Coalfield, Madhya Pradesh, India[28,33]

age	formation	max. thickness	lithology
early Eocene−late Cretaceous	Deccan Trap	100 m	dolerite dyke, basic flow
late Cretaceous	Lameta	25 m	sandstone and limestone
early Jurassic−late Triassic	Parsora	100 m	arenite interbedded with clay beds
early Triassic−late Permian	Pali	250 m	sandstone with clay matrix, coal seams
late Permian	Raniganj	550 m	sandstone alternating with claystone, coal and shale
		Local Disconformity	
late Permian	Barren measures	250 m	sandstone interbedded with siltstone, claystone and shale
		Local Disconformity	
early Permian	Barakar	265 m	sandstone, shale, claystone and coal seams
early Permian	Talchir	120 m	sandstone, quartz, rock fragment, claystone and shale
		Unconformity	
Precambrian	Surguja crystalline complex		

2.3. Determination of Organic and Mineral Composition. The mineral composition of coal is determined using Malvern Panalytical's Empyrean X-ray diffractometer. It is equipped with a Cu cathode and can function up to a maximum voltage of 40 kV. 10−15 mg of powdered (<75 μm) sample was used for analysis and was scanned from 5 to 70° 2θ angle with a scan step size of 0.02°/s. X-ray pattern analysis was performed using bundled HighScore Xpert Pro software.

Rock-Eval geochemical screening technique is a proven tool for determining thermal maturity, kerogen type, and source rock potential of organic-sedimentary rocks. Approximately 5 mg of coal samples, crushed to 212 μm are used for Rock-Eval, for reliable measurement of TOC.[35,36] Samples were analyzed with the incorporated basic/bulk rock method using Rock-Eval

6 instrument. Initially, the samples are heated in an inert atmosphere inside the pyrolysis oven of the Rock-Eval 6 device under isothermal conditions (300 °C) during which the free/adsorbed hydrocarbons within the samples are released and denoted as S1. Following the isothermal stage, programmed heating is performed to release the heavier hydrocarbons through thermal cracking by heating at a rate of 25 °C/min from 300 to 650 °C, in the same pyrolysis oven, and are denoted as S2. The temperature peak at which the greatest amount of hydrocarbon is cracked under S2 is noted as T_{max}. The samples are then moved from the pyrolysis oven to the oxidation oven, where they are once more heated from 300 °C until all of their remaining organic matter has been burned off, producing the residual carbon (RC) fraction. The PC and RC are added to determine the TOC content.[37] Other important calculated parameters are the hydrogen index [HI; (S2/TOC)×100], oxygen index [OI; (S3/TOC)×100].

2.4. LPGA Using CO_2 and N_2. LPGA was performed using a single station Quantachrome Autosorb iQ physisorption equipment. 1−2 gm of powdered sample was used for each run. To remove adsorbed moisture and volatile matter, samples were initially degassed at 110 °C for 600 min at 10^{-4} Torr pressure in vacuum condition.[21,38] N_2 and CO_2 were used as adsorbates for analyzing micropores and mesopores, respectively. N_2 is an inert gas that does not react; it is also easily available and hence widely used for mesopore adsorption experiments.[39] Numerous investigations have shown that specific surface area (SSA) determined using N_2 at 77 K is underestimated. Gan et al.[40] investigated that SSA calculated using N_2 is very low (<1 m²/g) except for a few high carbon containing (TOC: 75−81%) coal samples showing SSA greater than 10 m²/g. However, there is no appreciable difference between the kinetic diameter of two molecules (N_2-0.36 nm and CO_2-0.33 nm) but the difference in adsorption capacities is notable. Due to the quadrupolar nature and diatomic molecular shape of N_2, it is not a reliable adsorptive for the evaluation of micropore filling. The higher operational temperature and strong affinity for polar surface class (zeolites/oxides) increases the accessibility of CO_2 to micropores.[41,42] Hence, CO_2 with a lower molecular size and higher experimental temperature than N_2 is used alternately; it has the potential to access micropores.[40,43] The combination of CO_2 and N_2 adsorption offers a full spectrum of pores from micro to macro pores.[44,45]

For N_2, isotherms were obtained at 77 K with relative pressure (P/P_0) ranging from 0 to 0.99. The Brunauer−Emmett−Teller (BET) theory is used to estimate SSA. Quenched surface density functional theory (QSDFT) was used to study PSD for mesopores only and total pore volume (TPV) is calculated using the Kelvin method. For CO_2, isotherms were obtained at 273 K with relative pressure (P/P_0) ranging from 0.0003 to 0.03. Micropore surface area (SSA) is estimated using the Dubinin−Radushkevich (DR) equation, micropore volume is obtained using Dubinin−Astakhov (DA) method, and CO_2-DFT-based PSD is analyzed using isotherm.

DFT is developed into a potent technique for physisorption interpretation and is accepted as the preferred method for PSD analysis.[46−50] In contrast to more traditional approaches, such as Barrett, Joyner, and Halenda (BJH) method, DFT is not dependent on capillary condensation and can be used for the entire micro−mesopore range. Non-Local DFT (NLDFT) is based on the well-established concepts of classical and statistical thermodynamics. It is assumed that, under specific

regulated circumstances, the adsorbate is in thermodynamic equilibrium with the adsorptive in the gas phase. This kernel-based model assumes the density-dependent spread of adsorbed fluid when calculating the PSD using adsorption–desorption isotherm data. The pore wall is assumed to be smooth by NLDFT, which can cause anomalies in the analysis at low pressure.[20] To overcome these limitations, QSDFT increases some degree of roughness to the pore surface.[50] However, the level of disorder in the QSDFT model might not exactly correspond to that of the solid itself. QSDFT method is limited to calculating the PSD up to 35−40 nm. Hence, the BJH method is used to measure the PSD up to 100 nm. In this study, the QSDFT and BJH approach is used to estimate the large spectrum of pore width.

Fractal dimension accounts for the heterogeneity of pore structures, it can describe the roughness factor of pore surface[51,52] and its influence on adsorption potential using N_2-LPGA (77 K) adsorption data. Various methods such as the Langmuir model, fractal BET model, thermodynamic method, and Frenkel−Halsey−Hill (FHH) model have been developed to compute the fractal dimension of porous media based on gas adsorption−desorption isotherm.[53−56] The FHH model, which bases its calculations on gas adsorption isotherms, is the most efficient way to determine the fractal dimension of coal and shale adsorption pores.[57,58] FHH model considers that adsorbate−adsorbate interactions are less dominant than substrate−adsorbate interactions, and hence, it is not eligible up to the outermost layer of the film. Distribution of range in fractal analysis is based on the concept of dimension in fractal geometry. In Euclidean geometry, a line has 1 dimension, a plane has 2 dimensions, and a three-dimensional space has a dimension of 3. However, fractal objects show complexity and self-similarity at different scales.[51] For self-similar fractals (i.e., fractals that repeat pattern at zooming level increases), the fractal dimension lies between 1 and 2. Complex fractals which shows additional features with increase in zooming levels have fractal dimensions in the range of 2−3. These fractals show interrelated structures and remarkable details at different scales. Complex fractal dimension value closer to 2 indicates a smooth surface, whereas roughness increases from 2 to 3, and 3 is considered as a highly rough surface.[52,56]

The widely used FHH model can be described using the equation[54]

$$\ln\left(\frac{V}{V_0}\right) = A\left[\ln\left(\ln\left(\frac{P_0}{P}\right)\right)\right] + C \tag{1}$$

where V—N_2 adsorbed volume at equilibrium pressure P, V_0—volume of gas adsorbed by the monolayer, P_0—N_2 saturation pressure (77 K), C—constant, and power law exponent A is reliant on fractal dimension (D). The difference between the isotherms at relative pressures of 0−0.5 and 0.5−1 reflects various adsorption properties.[55] Due to extremely low surface tension, the Van der Waals force regulates the way that adsorbate and adsorbent interact at very low P/P_0 (0.5 > P/P_0 > 0.01), resulting in the following correlation between A and D[53,54]

$$A = D_1 + 3 \tag{2}$$

$$D_1 = A + 3 \tag{3}$$

with the increase in surface tension, adsorbate−adsorbent interactions between coarser mesopores and macropores (0.99

> P/P_0 > 0.5), are governed by capillary condensation and the equation is modified as follows[53,54]

$$A = \frac{D_2 - 3}{3} \tag{4}$$

$$D_2 = 3A + 3 \tag{5}$$

$\ln V$ vs $\ln[\ln(P_0/P)]$ FHH plot is plotted and their slope (A) of the curve is used for the calculation of D using the above two equations. At P_0/P of 0.5, the FHH fractal curve is divided into two parts: D_1 and D_2. D_1 and D_2 are used to describe the intricacy of pore structure and surface.[57]

N_2-LPGA-derived FHH fractal dimension values D_1 and D_2, are computed using eqs 3 and 5. Values obtained using eq 5 are found to be unfeasible, lower than 2 which disagrees with the described range of complex fractal dimension values (2−3). Hence, values obtained using eq 3 seems to be more appropriate for both segments D_1 and D_2.[59−61]

2.5. FEG-SEM Imaging. FEG-SEM is the most widely accepted method of observing pore features and organic matter in coal and shale samples. Flat flakes of approximately 10 × 10 × 1 mm are recovered from samples and further air dried at 80 °C before SEM imaging. Coal and shale are non-conductive materials. Its surface functions as an electron trap and extra white spots can be observed on the sample due to charging, a build-up of electrons on the surface that might tamper with imaging findings. Because the conductive coating provides a pathway for ejecting the material's charged electrons, application of sputter coater is recommended to get a high-quality electron image. In the present study, samples are coated with a thin layer of platinum (∼10 nm) to enhance the conductivity. Double-sided carbon tape is used to attach coated samples to the stage. JOEL JSM-7600F FEG-SEM instrument was used for acquiring high-resolution pore images.

2.6. Small Angle X-ray Scattering. SAXS is a method for analytical characterization that is used to identify the structure of particle systems based on their typical sizes or shapes. X-rays scatter due to the scattering contrast produced by different components in the material. These changes typically reflect the sample's chemical heterogeneity and differences in density. Significant contrast in matrix and pore space can be observed for X-rays. In the present study, Xenocs Xeuss 2.0 instrument was used for obtaining SAXS measurements. GeniX3D Cu source having 30 W Cu tube with 50 kV and 0.6 mA current is used. An EIGER R 1M detector with a 75 μm pixel size is used for collecting data. XSACT software by Xenocs is utilized for basic data processing. The sample-to-detector distance was set at around 6 m, and the powder coal samples were packed in Kapton tape to maintain the consistency of sample thickness and volume across measurements. Intensity is normalized against the thickness of each sample. For the selected experimental setup, the available Q-range was between 0.04 and 1.5 nm^{-1}. Raw data files obtained are processed using MATSAS Matlab module by Rezaeyan et al.[62] Details of calculation are also mentioned in Chandra et al.[17,23]

Fractal dimension derived from the SAXS can be described with the following equation[17]

$$D_S = 6 - A \tag{6}$$

where D_S is surface fractal dimension calculated from SAXS data and A is the slope of $I(Q)$ versus Q plot.

Table 2. Mineral Composition and Kerogen Characteristics of the Studied Coals

sample	depth (m)	mineral composition				kerogen characteristics					
		quartz (%)	clay mineral (%)	siderite (%)	mica (%)	S1 (mg/g)	S2 (mg/g)	TOC (wt %)	T_{max} (°C)	HI (mg HC/g of TOC)	OI (mg CO_2/g of TOC)
SGP-220	220	79	21	0	0	0.45	68.60	27.96	438	245	10
SGP-301	301	76	24	0	0	0.90	63.98	45.33	432	141	17
SGP-506	506	63	37	0	0	1.20	10.86	17.65	445	102	13
SGP-723	723	69	29	2	0	4.09	131.04	52.02	442	211	8
SGP-848	848	72	24	3	1	4.10	124.01	67.98	439	182	7

3. RESULTS AND DISCUSSION

3.1. Compositional Characteristics of Coal. The mineral composition of coal samples shows the dominance of quartz followed by clay minerals with low abundance of siderite and mica in some cases. TOC varies in the range of 17.65−67.98 wt % (Table 2). Samples SGP-220 and SGP-506 were observed to be marked by TOC contents of 27.96 and 17.65 wt %, indicating them to be coaly shale and carbonaceous shale, respectively. For the coal samples, the TOC content was observed to vary between 45.33 and 67.98 wt %. Samples SGP-723 and SGP-848 were observed to be marked by very high S1 values (that is free/adsorbed hydrocarbons) of 4.09 and 4.10 mg HC/g rock. It thus indicates them to be "excellent" sources for free hydrocarbons or gas plays.[25] Similarly, with S1 of 1.20 mg HC/g rock, sample SGP-506 can be categorized under "good" source for free hydrocarbons or gas plays.[25] The T_{max} of the studied suite of samples, was observed to vary between 432 and 445 °C, indicating them to be at the early mature stage of thermal maturity.[25] The variation in HI for the studied suite of samples indicates input of dominantly type III kerogen and type II-III admixed kerogen (SGP-220 and SGP-723) at places. Figure 2 plots the pseudo van Krevelen diagram, indicating the same.
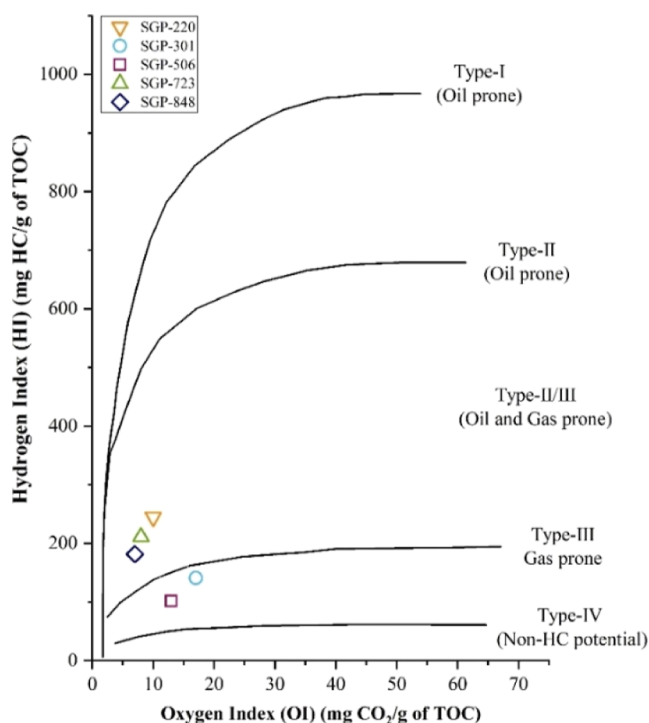

**Figure 2.** Pseudo van Krevelen diagram showing the gas generation potential of Sohagpur coalfield samples.

3.2. Pore Characterization. *3.2.1. FEG-SEM High-Resolution Imaging.* High-resolution FEG-SEM images of coal and shale depict the two-dimensional morphology of pores and offer vital details regarding their shape. SAXS and LPGA are quantitative methods that can quantify the pore dimensions and frequency but cannot describe the morphology of the pore. Highly heterogeneous surface, mineral matter, and organic matter produce a charging effect, which makes it challenging to capture pores less than 5 nm.

The pores range in size from 5 to 70 nm. Pores show distinct shapes with rough and undulating aperture areas. Organic matter contributes a majority of the part in coal composition; hence, most of the pores are enclosed in organic matter. Loucks et al.[63] classified matrix related pores as (i) organic pores, (ii) interparticle pores (interP)- pores formed by the vacant space between mineral particles, and (iii) intraparticle pores (intraP)- pores formed by voids within the mineral particles. Prominent OM pores in clustered form are shown in Figure 3a,b, showing spherical to irregular shapes. Concentric lines along the aperture of spherical-semispherical pores in Figure 3b indicate the interconnectivity of pores with the above part. Intergranular pores can be formed between clastic particles (quartz) Figure 3c,f,g, clastic (quartz)-nonclastic (clay minerals) particles (Figure 3d), and nonclastic−nonclastic material (Figure 3d). Elongated intraparticle pores are visible in Figure 3f. Interlayer pores[13] are formed by the void between the layers (Figure 3e). A slit-type elongated pore is formed between the elongated mineral grains Figure 3d,e,h.

3.2.2. SEM Image Analysis. Quantitative methods like LPGA and SAXS are more reliable in analyzing pore dimensions and pore frequency. SEM images visually validate pore shapes and sizes for a specifically selected area. It is very difficult and uneconomic to cover the entire section under SEM; hence, some representative areas with prominent pore visualization are captured. SEM images captured vary with magnification, lens working distance, resolution, and surface coating, which will vary each time with the operator's adjustment. However, it is essential to validate the pore size distribution data of SEM images with quantitative methods (LPGA and SAXS) data. Image analysis is performed to validate the SEM pore size distribution with quantitative methods.

Since the representative SEM images depict a small portion of the sample, the estimation of pore size distribution is limited to a certain extent. Porosity and pore size distribution are analyzed using a MATLAB-based script described by Rabbani and Salehi[64] and Ezeakacha et al.[65] Figure 4a is the raw SEM image of the coaly shale sample. Figure 4b represents the intensity map of the raw SEM image obtained by Otsu multi-level thresholding[66] with 6-level quantization, this helps to determine the pore spaces with greater accuracy. Figure 4c shows the darkest portion marked in black pixels with a white
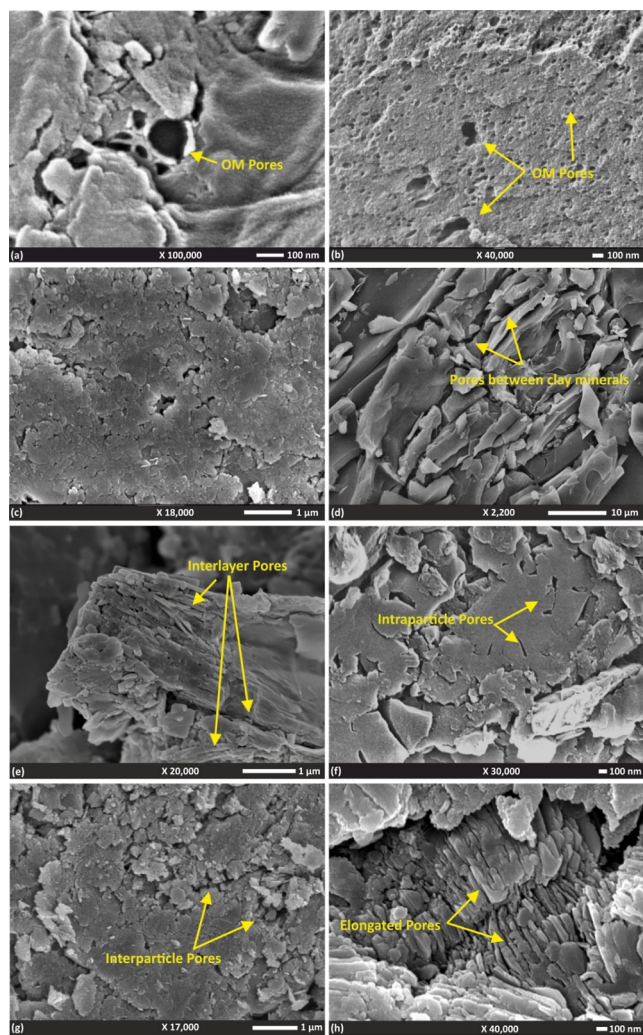
Figure 3. SEM images of coal samples showing variation in pore types with depth and composition (a,b) SGP-220, (d) SGP-506, (e,g) SGP-301, (c,f) SGP-723, and (h) SGP-848.

background. Figure 4d represents the segmentation of pore spaces using the Watershed segmentation algorithm. Segmented pore spaces are labeled with random color schemes. City block distance transform along with the noise-reduction technique of median filtering is utilized in the Watershed segmentation process, it can accurately identify and distinguish overlapped porous geometries to get the average pore size.[67,68] SEM images with distinct and prominent pore types and minimum magnification differences are chosen for image analysis. Figure 3b,f−h is considered for image analysis.
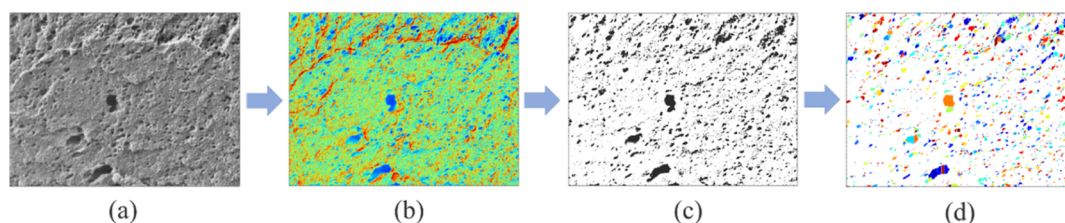
Calculated porosities from SEM images by image analysis vary in the range of 12−17%. Maximum porosity is measured for Figure 3h due to the formation of numerous elongated pores. Also, interlayer porosity contributes significantly to Figure 3h. Figure 3b shows minimum porosity.
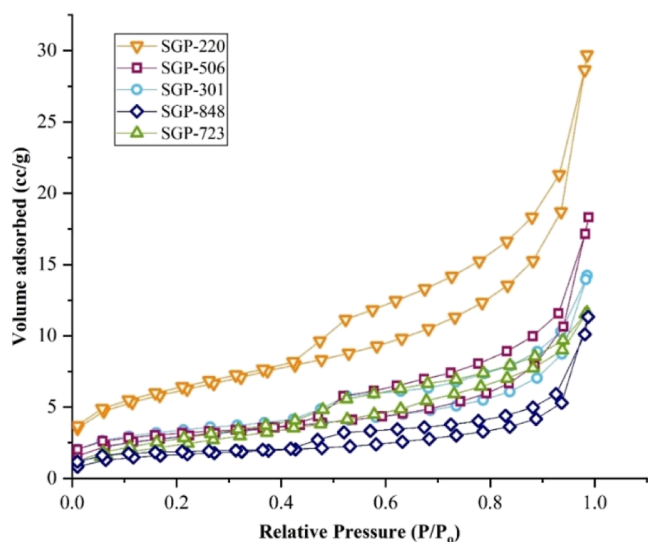
Figure 5 represents the PSD trend from SEM images; the frequency plot depicts the dominance of pores in the range of
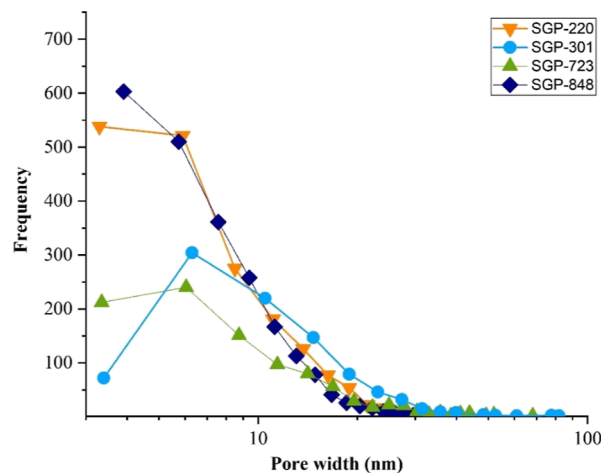
Figure 5. Frequency distribution of pore width estimated using image analysis.

2.5−10 nm in all the samples. Figure 5 illustrates the higher pore count for SGP-220 (Figure 3b) and SGP-848 (Figure 3h) in the range of 3−6 nm, owing to a large number of OM pores and elongated pores. SGP-723 (Figure 3f) and SGP-848 (Figure 3g) with the dominance of interparticle and intraparticle pores show lower pore count due to irregular pore size distribution and higher mineral content.

3.2.3. N$_2$-LPGA Mesopore Characterization. In the N$_2$ isotherm, type IV isotherm (IUPAC classification) is observed, indicating the presence of mesopores in the material. The hysteresis curve formed between the adsorption curve and desorption curve is H3 to H4 type, confirming the presence of slit type and ink bottle type of pores, as shown in SEM images (Figure 3). The most common isotherm is type IV, which is typical of mesoporous substances and progresses through monolayer and multilayer hysteresis before capillary condensation during desorption.[69] An abrupt drop in the adsorbed gas volume along the desorption curve between P/P_0 0.42 and 0.52 indicates the tensile strength effect (TSE) caused by the cavitation in slit type and ink bottle pores. The TSE is prominent in the shallow depth samples and gradually declines with the depth as shown in Figure 6. TSE is more noticeable in coaly and carbonaceous shale (SGP-220 and SGP-506) compared to other coal samples.

Figure 4. SEM image analysis of Figure 3b. (a) SEM image of coaly shale, (b) intensity map of SEM image, (c) detected pore space, and (d) segmentation of pore space.

Figure 6. N_2 adsorption—desorption isotherm of coal and shale samples at 77 K.

Figure 7. CO_2 adsorption isotherm of Sohagpur coal samples at 273 K.

The mean BET surface area for the studied samples is 11.42 m^2/g, with the highest BET SA of 21.64 m^2/g shown by SGP-220 and the lowest BET SA of 5.79 m^2/g shown by SGP-848. N_2 isotherm represents the lowest volume of gas adsorbed for SGP-848 and the highest for SGP-220, with a steady decrease in the volume of gas adsorbed with depth except for SGP-506. The calculated average TPV is 0.02 (cc/g), with the maximum estimated volume of 0.039 (cc/g) represented by SGP-220 and a minimum volume of 0.014 cc/g shown by SGP-848 (Table 3).

Table 3. Mesopore and Micropore Characteristics Estimated Using N_2 and CO_2 Isotherm

sample	mesopore data		micropore data	
	BET surface area (m^2/g)	DFT pore volume (cc/g)	DR surface area (m^2/g)	DA pore volume (cc/g)
SGP-220	21.64	0.039	58.98	0.036
SGP-301	10.02	0.018	120.13	0.053
SGP-506	10.33	0.023	73.43	0.057
SGP-723	9.31	0.016	119.76	0.066
SGP-848	5.79	0.014	130.08	0.057

3.2.4. CO_2-LPGA Micropore Characterization. CO_2 adsorption isotherm of Sohagpur coal and shale samples shows type I adsorption isotherm (Figure 7), indicating microporous material. At low relative pressures (0.001—0.007), samples show higher adsorption potential (Figure 7).

Micropore surface area (SA) and micropore volume (PV) is calculated using the DR and DA method, respectively. The calculated DR surface area for micropore is in the range of 58.98—130.08 m^2/g, with SGP-220 showing the lowest SA and SGP-848 marking the highest SA. DA pore volume varies from 0.036 to 0.066 cc/g, the lowest PV is shown by SGP-220 and the highest by SGP-723 (Table 3).

3.2.5. Correlation of Depth and TOC with SA, PV. Figure 8a shows the cross-correlation of DA micropore volume and DFT mesopore volume with TOC (wt %) and Figure 8b DR micropore surface area and MBET mesopore surface area with TOC. With the increase in TOC, a significant decrease in
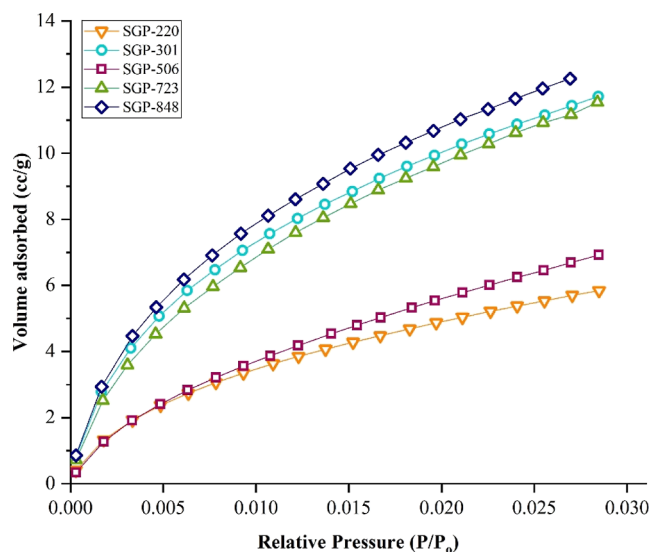
mesopore volume and surface area is observed, whereas micropore volume and surface area shows positive correlation with TOC. SGP-506 shows anomalous behavior due to its lowest TOC (Table 2), indicating the influence of TOC on surface area of pore and pore volume estimation.

Micropore surface area and pore volume are showing a positive correlation with the depth however mesopore surface area and pore volume depicts a negative correlation with the depth (Figure 9). Increasing overburden pressure with depth may cause compression of the pores resulting in the decrease in mesopores. Also, overburden pressure initiates the migration of clay minerals into the pores. Due to the larger pore width of mesopores, clay primarily enters into mesopores and induces clogging in pores, whereas the entry of clay minerals in micropores is restricted due to its smaller pore widths.

3.2.6. Pore Size Distribution Estimated Using LPGA. Figure 10a shows the merged N_2 and CO_2 (DFT) pore size distribution for Sohagpur coal and shale samples. CO_2 DFT pore size distribution (Figure 10a) shows distinct peaks around 0.35, 0.5, and 0.8 nm pore width. Shallower depth samples (i.e., SGP-220) show that major volume is contributed by mesopores, whereas micropores contributes significantly for higher depth samples (i.e., SGP-723, 848).

N_2-mesopore PSD shows the highest mesopore volume for SGP-220 and minimum for deepest samples- SGP-723 and SGP-848. Peaks are observed around 3—5, 10—12, and 21—22 nm. The average pore diameter is in the range of 8.49—12.10 nm, showing a progressively increasing trend with depth. Figure 10b shows BJH PSD, SGP-220 illustrates maximum pore volume, and SGP-848 shows minimum pore volume, which is also reflected in the N_2 isotherm graph (Figure 6).

3.2.7. N_2-LPGA-Derived Fractal Dimension. FHH fractal dimension plots for coal and shale samples are available in the Supporting Information.

Correlation coefficient values are higher than 0.95, suggesting that the coal sample possesses fractal properties. Fractal dimension values for D_1 (smaller mesopores) are greater compared to D_2 (larger mesopores), pointing to the higher surface roughness of smaller mesopores (Table 4). D_N is the average fractal value of D_1 and D_2, it ranges from 2.52 to 2.63, and reflects the variety of surfaces that may be used to

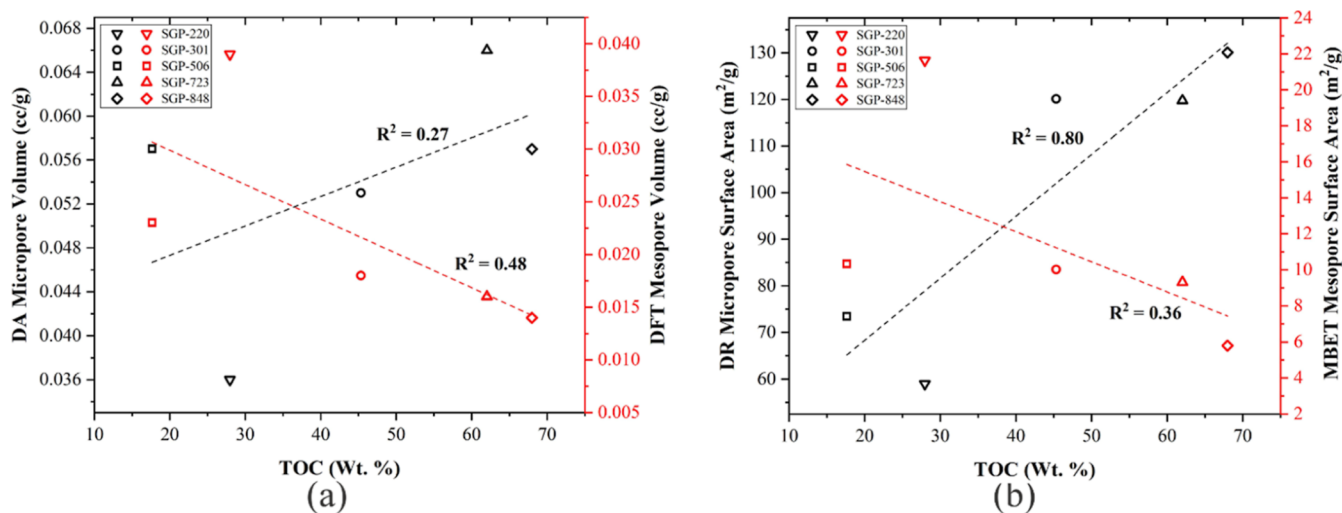**Figure 8.** (a) Impact of TOC (%) over the pore volume and (b) impact of TOC (%) over the surface area of samples.
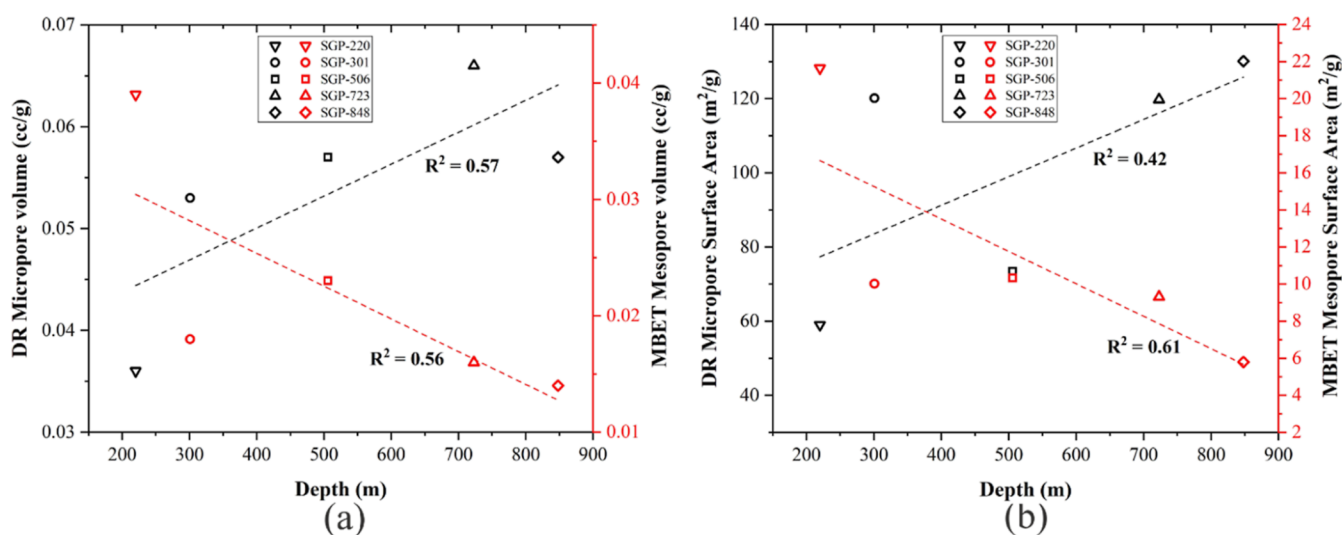

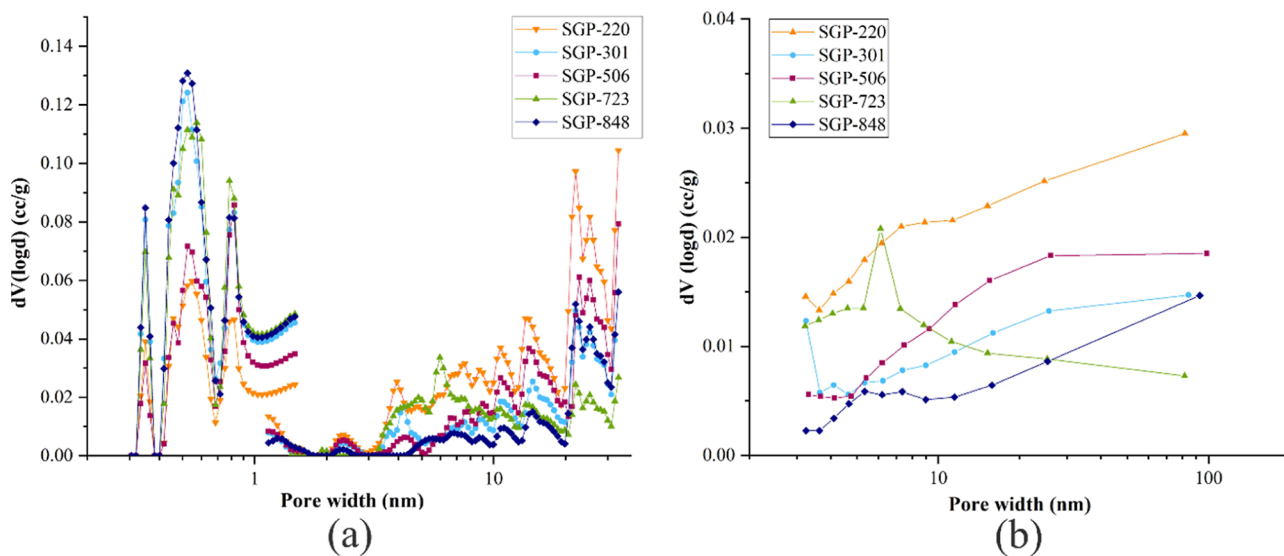**Figure 9.** (a) Influence of depth on pore volume and (b) influence of depth on the surface area of samples.

Figure 10. (a) Merged micropore (CO_2: 0.2 to 2 nm) and mesopore (N_2: 1.44 to 35 nm) DFT PSD of coal and shale samples and (b) BJH PSD of coal and shale samples (up to 100 nm).

Table 4. N$_2$-LPGA-Derived FHH Fractal Dimension of Sohagpur Coalfield Samples

sample	(0.5 > P/P$_0$ > 0.01)			(0.98 > P/P$_0$ > 0.5)			
	slope (A)	R^2	D$_1$ = 3 + A	slope (A)	R^2	D$_2$ = 3 + A	D$_N$ = D$_1$ + D$_2$/2
SGP-220	−0.32	0.99	**2.68**	−0.47	0.99	**2.53**	**2.605**
SGP-301	−0.33	0.99	**2.67**	−0.47	0.98	**2.53**	**2.6**
SGP-506	−0.38	0.99	**2.62**	−0.47	0.97	**2.53**	**2.575**
SGP-723	−0.27	0.95	**2.73**	−0.68	0.99	**2.32**	**2.525**
SGP-848	−0.4	0.99	**2.6**	−0.33	0.99	**2.67**	**2.635**
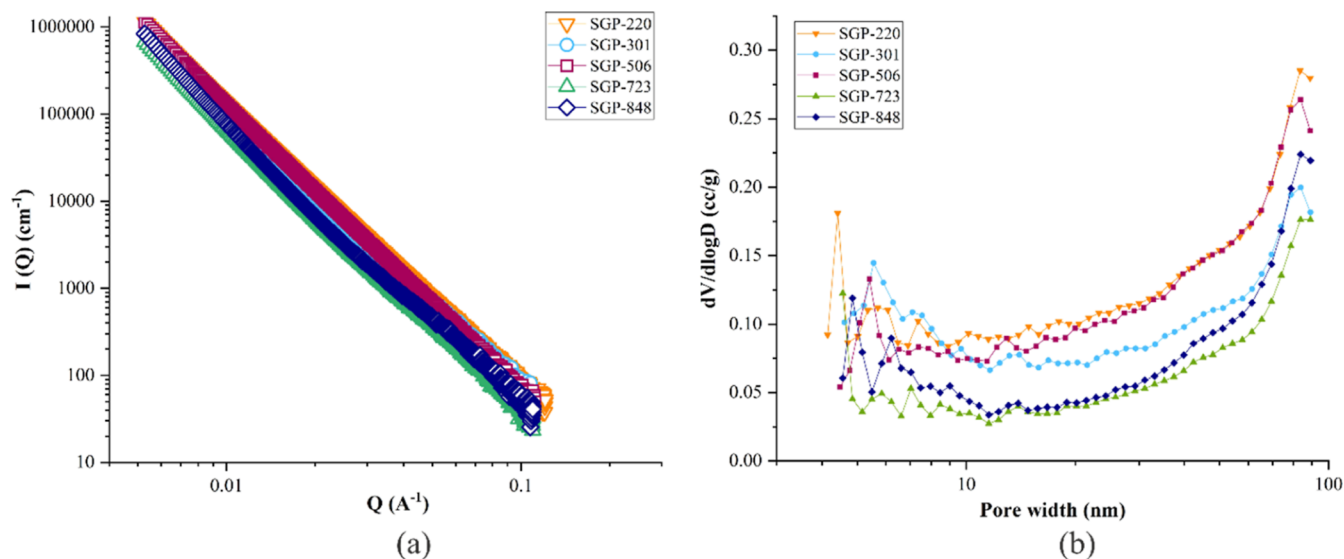
Figure 11. (a) Scattering vector (Q) vs intensity (b) PSD estimated using SAXS (PDSP model).

store gas. An increase in mesopore volume and surface area is observed with the increase in surface roughness. While comparing the composition with surface roughness, surface roughness correlates positively with TOC content, whereas clay content exhibits a negative correlation.

3.2.8. X-ray Scattering Based Pore Attributes. SAXS is widely used nowadays for characterizing pore attributes from rocks. Advanced SAS instruments can provide a wide range of accessible pores from ~2 nm to 20 μm. This is a good alternative to fluid probing methods like LPGA and can be performed on whole samples as well as crushed samples. In this study, powdered coal and shale samples are used for SAXS analysis.

Pore characterization from the SAXS data is carried out with the help of a Matlab module-MATSAS. The polydisperse Spherical Model (PDSP) is utilized for estimating PSD, which accurately measures PSD for randomly oriented scattering granules. SAXS raw data file containing scattering vector (Q) and intensity along with calculated scattering length density (SLD) values and sample densities is fed into MATLAB program using a .csv file. SLD is assumed to be zero for void space.

Scattering intensity (I) for an ideal PDSP scatter is defined as:[70,71]

$$I(Q) = \sum_n C_n \int_{R_{min}}^{R_{max}} r^6 P(Q, r) f(r, D_n, R_{max}, R_{min}) dr$$

(7)

where C_n is a constant independent of Q

$$P(Q, r) = \left[3 \frac{\sin(Q, r) - Qr \cos(Q, r)}{Q^3 r^3} \right]^2$$

(8)

and $f(r, D_n, R_{max}, R_{min})$ is power-law PSD for nth contribution, which is defined as

$$f(r, D_n, R_{max}, R_{min}) = \frac{[r^{-(1+D_n)}]}{\left[\frac{R_{min}^{-D_n} - R_{max}^{-D_n}}{D_n} \right]}$$

(9)

Further calculations of SSA and PSD are explained by Rezaeyan et al.[62]

3.2.9. Power-Law PSD. Figure 11a shows the plot of intensity plotted against the scattering vector. The scanned SAXS profile (Figure 11a) shows striking similarity with each other signifying low heterogeneity. PSD for all the samples shows similar trends with higher pore volumes in lower (<10 nm) and higher mesopore (>10 nm) ranges.

The significant difference between the pore volumes of all five samples can be observed between 10 and 11 nm. Major peaks in lower mesopore volume are observed around 4 to 7 nm and around 80 to 90 nm for the higher mesopore range, which shows consistent results with BJH PSD. SAXS mesopore PSD (Figure 11b) depicts decreasing PV trend with the depth. SAXS PSD shows the mesopore volume peaks in lower and higher mesopore ranges, whereas LPGA-derived PSD (Figure 10) shows a significant increase in pore volume with the increase in pore width beyond 10 nm. The absence of pore volume peaks in the N$_2$-LPGA derived PSD is due to the inaccessibility of N$_2$ into the pores less than 10 nm, underestimating the TPV.

3.2.10. Scattering-Based Surface Fractal Analysis. In general, surface fractal dimension (D_S) values derived from SAXS are higher over LPGA estimated fractal values (D_N). Higher values of D_S indicate greater surface roughness of inaccessible pores (finer pores) compared to accessible pores (coarser pores). In natural porous systems, finer pores are larger in number relative to coarser pores. Coal and shale pore system have poor connectivity, and it reduces further in the case of finer pores, which becomes one of the major limitation for total porosity estimation with gas adsorption method. Figure 12 shows the combined PSD of N_2-LPGA-derived BJH
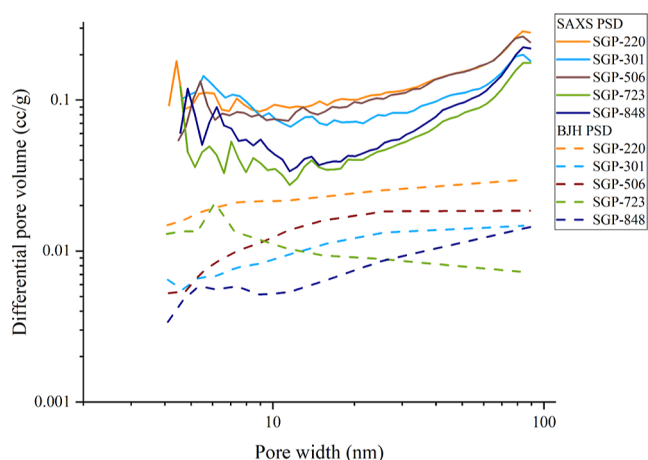
Figure 12. Combined PSD of SAXS and N_2-LPGA derived BJH PSD.

PSD and SAXS PSD. SAXS PSD shows the notable pore volume in the finer mesopore range of 2−10 nm, whereas these peaks are missing in BJH PSD. Primarily this is due to inability of N_2 to access finer mesopores, which underestimates the LPGA calculated pore volume. PV estimated with SAXS is up to 62% higher compared to LPGA-derived BJH PV (Table 5). Similarly, larger pore surface area values are observed for SAXS SA relative to LPGA-derived SA.

Table 5. Comparison of Mesopore Volumes and Fractal Dimension Estimated Using N_2-LPGA and SAXS

sample	fractal dimension		mesopore volume		
	N_2-LPGA D_N	SAXS D_S	N_2-LPGA	SAXS	percent change (%)
SGP-220	2.60	2.75	0.037	0.060	62.2
SGP-301	2.6	2.79	0.015	0.017	13.3
SGP-506	2.57	2.69	0.023	0.028	21.7
SGP-723	2.52	2.57	0.011	0.015	36.4
SGP-848	2.63	2.51	0.015	0.019	26.7

4. CONCLUSIONS

This study of Sohagpur coalfield, Madhya Pradesh, India investigates coal and shale composition and detailed pore characterization using a combination of LPGA, SAXS, and FEG-SEM for exploring prospects of enhanced CBM recovery in the coalfield. Significant conclusions derived from the study are as follows:

(a) The marginally mature nature of Sohagpur samples and type II/III kerogen indicates the ECBM prospective in the coalfield.

(b) In general, mesopore volume and surface area decrease with an increase in TOC content, while an inverse trend is observed for micropore surface area and pore volume. Clay content shows a moderate influence on micropores but depicts a strong negative trend over mesopore volume and surface area.

(c) Sohagpur coalfield samples show a decrease in mesopore SA and PV of around 273 and 178% with depth. Micropore data depict an increase in SA and PV with depth by up to 120 and 83%, respectively. More number of micropores facilitates a larger surface area for gas adsorption.

(d) Surface roughness correlates positively with TOC content, whereas it shows a negative trend with clay content.

(e) SAXS derives surface fractal dimension (D_S) shows notably high values compared to N_2-LPGA-derived fractal dimension (D_N) due to the incorporation of inaccessible pores. Inaccessible pores have more surface roughness than accessible pores. Surface roughness is directly proportional to pore volume (up to 62%) and surface area.

■ ASSOCIATED CONTENT

Ⓢ Supporting Information

The Supporting Information is available free of charge at https://pubs.acs.org/doi/10.1021/acs.energyfuels.3c01007.

FHH fractional dimension plot for all samples (PDF)

■ AUTHOR INFORMATION

Corresponding Author

Sarada Prasad Pradhan − *Department of Earth Sciences, IIT Roorkee, Roorkee 247667, India;* ⓘ orcid.org/0000-0001-5054-4370; Email: sppradhan@es.iitr.ac.in

Authors

Pranay Vilas Bhapkar − *Department of Earth Sciences, IIT Roorkee, Roorkee 247667, India*

Debanjan Chandra − *Department of Geoscience and Engineering, Delft University of Technology, Delft 2628 CN, the Netherlands;* ⓘ orcid.org/0000-0001-6093-7389

Bodhisatwa Hazra − *CSIR- Central Institute of Mining and Fuel Research, Dhanbad 826015, India;* ⓘ orcid.org/0000-0002-3462-7552

Vikram Vishal − *Computational and Experimental Geomechanics Laboratory, Department of Earth Sciences, IIT Bombay, Mumbai 400076, India; National Centre of Excellence in Carbon Capture and Utilization, IIT Bombay, Mumbai 400076, India;* ⓘ orcid.org/0000-0002-0896-7844

Complete contact information is available at:
https://pubs.acs.org/10.1021/acs.energyfuels.3c01007

Notes

The authors declare no competing financial interest.

Centre of Excellence in Carbon Capture and Utilization at IIT Bombay, Mumbai.

■ REFERENCES

(1) Dheeraj, D. *Coal Bed Methane by Application (Industrial, Power Generation, Transportation, Commercial, and Residential)—Global Opportunity Analysis and Industry Forecast, 2017-2023*; Allied Market Research, 2017. https://www.alliedmarketresearch.com/coal-bed-methane-CBM-market.

(2) Vishal, V.; Verma, Y.; Chandra, D.; Ashok, D. A Systematic Capacity Assessment and Classification of Geologic CO_2 Storage Systems in India. *Int. J. Greenh. Gas Control* **2021**, *111*, 103458.

(3) Vishal, V.; Chandra, D.; Singh, U.; Verma, Y. Understanding Initial Opportunities and Key Challenges for CCUS Deployment in India at Scale. *Resour. Conserv. Recycl.* **2021**, *175*, 105829.

(4) Mastalerz, M.; Hampton, L.; Drobniak, A.; Loope, H. Significance of Analytical Particle Size in Low-Pressure N_2 and CO_2 Adsorption of Coal and Shale. *Int. J. Coal Geol.* **2017**, *178*, 122−131.

(5) Karayigit, A. I.; Oskay, R. G.; Bulut, Y.; Mastalerz, M. Meso- and Microporosity Characteristics of Miocene Lignite and Subbituminous Coals in the Kinik Coalfield (Soma Basin, W. Turkey). *Int. J. Coal Geol.* **2020**, *232*, 103624.

(6) Chandra, D.; Vishal, V.; Bahadur, J.; Sen, D. A Novel Approach to Identify Accessible and Inaccessible Pores in Gas Shales Using Combined Low-Pressure Sorption and SAXS/SANS Analysis. *Int. J. Coal Geol.* **2020**, *228*, 103556.

(7) Mastalerz, M.; Drobniak, A.; Rupp, J. Meso- and Micropore Characteristics of Coal Lithotypes: Implications for CO_2 Adsorption. *Energy Fuel.* **2008**, *22*, 4049−4061.

(8) Mastalerz, M.; Goodman, A.; Chirdon, D. Coal Lithotypes before, during, and after Exposure to CO_2: Insights from Direct Fourier Transform Infrared Investigation. *Energy Fuel.* **2012**, *26*, 3586−3591.

(9) Busch, A.; Gensterblum, Y. CBM and CO_2-ECBM Related Sorption Processes in Coal: A Review. *Int. J. Coal Geol.* **2011**, *87*, 49−71.

(10) Rodrigues, C. F.; Lemos de Sousa, M. J. The Measurement of Coal Porosity with Different Gases. *Int. J. Coal Geol.* **2002**, *48*, 245−251.

(11) Swanson, S. M.; Mastalerz, M. D.; Engle, M. A.; Valentine, B. J.; Warwick, P. D.; Hackley, P. C.; Belkin, H. E. Pore Characteristics of Wilcox Group Coal, US Gulf Coast Region: Implications for the Occurrence of Coalbed Gas. *Int. J. Coal Geol.* **2015**, *139*, 80−94.

(12) Cai, Y.; Liu, D.; Pan, Z.; Yao, Y.; Li, J.; Qiu, Y. Pore Structure and Its Impact on CH_4 Adsorption Capacity and Flow Capability of Bituminous and Subbituminous Coals from Northeast China. *Fuel* **2013**, *103*, 258−268.

(13) Mays, T. J. A new classification of pore sizes. *Stud. Surf. Sci. Catal.* **2007**, *160*, 57−62.

(14) Curtis, M. E.; Sondergeld, C. H.; Ambrose, R. J.; Rai, C. S. Microstructural Investigation of Gas Shales in Two and Three Dimensions Using Nanometer-Scale Resolution Imaging. *Am. Assoc. Pet. Geol. Bull.* **2012**, *96*, 665−677.

(15) Chandra, D.; Bakshi, T.; Bahadur, J.; Hazra, B.; Vishal, V.; Kumar, S.; Sen, D.; Singh, T. N. Pore Morphology in Thermally-Treated Shales and Its Implication on CO2 Storage Applications: A Gas Sorption, SEM and Small-Angle Scattering Study. *Fuel* **2023**, *331*, 125877.

(16) Zhang, M.; Fu, X.; Zhang, Q.; Cheng, W. Research on the Organic Geochemical and Mineral Composition Properties and Its Influence on Pore Structure of Coal-Measure Shales in Yushe-Wuxiang Block, South Central Qinshui Basin, China. *J. Pet. Sci. Eng.* **2019**, *173*, 1065−1079.

(17) Chandra, D.; Vishal, V.; Bahadur, J.; Agrawal, A. K.; Das, A.; Hazra, B.; Sen, D. Nano-scale physicochemical attributes and their impact on pore heterogeneity in shale. *Fuel* **2022**, *314*, 123070.

(18) Yang, C.; Zhang, J.; Tang, X.; Ding, J.; Zhao, Q.; Dang, W.; Chen, H.; Su, Y.; Li, B.; Lu, D. Comparative Study on Micro-Pore Structure of Marine, Terrestrial, and Transitional Shales in Key Areas, China. *Int. J. Coal Geol.* **2017**, *171*, 76−92.

(19) Sun, M.; Yu, B.; Hu, Q.; Yang, R.; Zhang, Y.; Li, B.; Melnichenko, Y. B.; Cheng, G. Pore Structure Characterization of Organic-Rich Niutitang Shale from China: Small Angle Neutron Scattering (SANS) Study. *Int. J. Coal Geol.* **2018**, *186*, 115−125.

(20) Vishal, V.; Chandra, D.; Bahadur, J.; Sen, D.; Hazra, B.; Mahanta, B.; Mani, D. Interpreting Pore Dimensions in Gas Shales Using a Combination of SEM Imaging, Small-Angle Neutron Scattering, and Low-Pressure Gas Adsorption. *Energy Fuel.* **2019**, *33*, 4835−4848.

(21) Holmes, R.; Rupp, E. C.; Vishal, V.; Wilcox, J. Selection of Shale Preparation Protocol and Outgas Procedures for Applications in Low-Pressure Analysis. *Energy Fuel.* **2017**, *31*, 9043−9051.

(22) Okolo, G. N.; Everson, R. C.; Neomagus, H. W. J. P.; Roberts, M. J.; Sakurovs, R. Comparing the Porosity and Surface Areas of Coal as Measured by Gas Adsorption, Mercury Intrusion and SAXS Techniques. *Fuel* **2015**, *141*, 293−304.

(23) Chandra, D.; Vishal, V. A Comparative Analysis of Pore Attributes of Sub-Bituminous Gondwana Coal from the Damodar and Wardha Valleys: Implication for Enhanced Coalbed Methane Recovery. *Energy Fuel.* **2022**, *36*, 6187−6197.

(24) Bahadur, J.; Chandra, D.; Das, A.; Vishal, V.; Agrawal, A. K.; Sen, D. Pore Anisotropy in Shale and Its Dependence on Thermal Maturity and Organic Carbon Content: A Scanning SAXS Study. *Int. J. Coal Geol.* **2023**, *273*, 104268.

(25) Peters, K. E.; Cassa, M. R. Applied Source Rock Geochemistry. In *The Petroleum System—From Source to Trap*; American Association of Petroleum Geologists, 1994; Vol. *93−120*. DOI: 10.1306/M60585C5.

(26) Tissot, B.; Durand, B.; Espitalie, J.; Combaz, A. Influence of Nature and Diagenesis of Organic Matter in Formation of Petroleum. *Am. Assoc. Pet. Geol. Bull.* **1974**, *58*, 499−506.

(27) Milici, R. C.; Mukhopadhyay, A.; Warwick, P. D.; Adhikari, S.; Landis, E. R.; Mukhopadhyay, S. K. *The Sohagpur Coalfield Project - A Collaborative Study of Potential Coking Coal Resources by the Geological Survey of India and the U.S. Geological Survey*; USGS Publications Warehouse, 2003; p 70195464.

(28) Mondal, D.; Ghosh, S.; Naveen, P.; Kumar, M.; Majumder, A.; Kumar Panda, A. An Integrated Study on the Geochemical, Geophysical and Geomechanical Characteristics of the Organic Deposits (Coal and CBM) of Eastern Sohagpur Coalfield, India. *Gondwana Res.* **2021**, *96*, 122−141.

(29) Rao, C. S. R. Coal Resources of Madhya Pradesh, Jammu and Kashmir. Coalfields of India, Mand-Raigarh Coalfield, Madhya Pradesh. *Bulletins of the Geological survey of India: Series A*; Geological Survey of India, 1983.

(30) Pareek, H. S. Petrographic, Chemical and Trace-Elemental Composition of the Coal of Sohagpur Coalfield, Madhya Pradesh, India. *Int. J. Coal Geol.* **1987**, *9*, 187−207.

(31) Kumar, M.; Tripathi, A. K.; Ghosh, S.; Ayush. Estimation of Permeability of Coal Seams Using Well-Logs and Analysis of CBM Gas Content in the Eastern Part of Sohagpur Coalfields, Central India. *Minetech* **2020**, *40*, 3−11.

(32) Karthikeyan, G.; Chand, J.; Chatterjee, R. Impact of Geomechanics in Coal Bed Methane Development and Production, Barakar Coals in Central India. *J. Pet. Sci. Eng.* **2020**, *194*, 107515.

(33) Agnihotri, D.; Tewari, R.; Pillai, S. S. K.; Jasper, A.; Uhl, D. Early Permian Glossopteris Flora from the Sharda Open Cast Mine, Sohagpur Coalfield, Shahdol District, Madhya Pradesh. *Palaeobotanist* **2016**, *65*, 97−107.

(34) Jasper, A.; Agnihotri, D.; Tewari, R.; Spiekermann, R.; Pires, E. F.; Da Rosa, Á. A. S.; Uhl, D. Fires in the Mire: Repeated Fire Events in Early Permian 'Peat Forming' Vegetation of India. *Geol. J.* **2016**, *52*, 955−969.

(35) Hazra, B.; Dutta, S.; Kumar, S. TOC Calculation of Organic Matter Rich Sediments Using Rock-Eval Pyrolysis: Critical Consideration and Insights. *Int. J. Coal Geol.* **2017**, *169*, 106−115.

(36) Hazra, B.; Karacan, C. O.; Tiwari, D. M.; Singh, P. K.; Singh, A. K. Insights from Rock-Eval Analysis on the Influence of Sample Weight on Hydrocarbon Generation from Lower Permian Organic Matter Rich Rocks, West Bokaro Basin, India. *Mar. Pet. Geol.* **2019**, *106*, 160−170.

(37) Behar, F.; Beaumont, V.; De B Penteado, H. L. Rock-Eval 6 Technology: Performances and Developments. *Oil Gas Sci. Technol.* **2001**, *56*, 111−134.

(38) Singh, D. P.; Chandra, D.; Vishal, V.; Hazra, B.; Sarkar, P. Impact of Degassing Time and Temperature on the Estimation of Pore Attributes in Shale. *Energy Fuel.* **2021**, *35*, 15628−15641.

(39) Eddaoudi, M. Characterization of Porous Solids and Powders: Surface Area, Pore Size and Density By S. Lowell (Quantachrome Instruments, Boynton Beach), J. E. Shields (C. W. Post Campus of Long Island University), M. A. Thomas, and M. Thommes (Quantachrome In-struments). Kluwer Academic Publishers: Dordrecht, The Netherlands. 2004. xiv + 348 pp. $159.00. ISBN 1-4020-2302-2. *J. Am. Chem. Soc.* **2005**, *127*, 14117.

(40) Gan, H.; Nandi, S. P.; Walker, P. Nature of the Porosity in American Coals. *Fuel* **1972**, *51*, 272−277.

(41) Thommes, M.; Cychosz, K. A. Physical Adsorption Characterization of Nanoporous Materials: Progress and Challenges. *Adsorption* **2014**, *20*, 233−250.

(42) Liu, Y.; Wilcox, J. Effects of Surface Heterogeneity on the Adsorption of $CO2$ in Microporous Carbons. *Environ. Sci. Technol.* **2012**, *46*, 1940−1947.

(43) Walker, P. L.; Verma, S. K.; Rivera-Utrilla, J.; Khan, M. R. A direct measurement of expansion in coals and macerais induced by carbon dioxide and methanol. *Fuel* **1988**, *67*, 719−726.

(44) Hazra, B.; Vishal, V.; Singh, D. P. Applicability of Low-Pressure CO_2 and N_2 Adsorption in Determining Pore Attributes of Organic-Rich Shales and Coals. *Energy Fuel.* **2021**, *35*, 456−464.

(45) Chandra, D.; Bakshi, T.; Vishal, V. Thermal Effect on Pore Characteristics of Shale under Inert and Oxic Environments: Insights on Pore Evolution. *Microporous Mesoporous Mater.* **2021**, *316*, 110969.

(46) Cracknell, R. F.; Gubbins, K. E.; Maddox, M.; Nicholson, D. Modeling Fluid Behavior in Well-Characterized Porous Materials. *Acc. Chem. Res.* **1995**, *28*, 281−288.

(47) Neimark, A. V.; Ravikovitch, P. I. Capillary Condensation in MMS and Pore Structure Characterization. *Microporous Mesoporous Mater.* **2001**, *44−45*, 697−707.

(48) Neimark, A. V.; Ravikovitch, P. I.; Vishnyakov, A. Bridging Scales from Molecular Simulations to Classical Thermodynamics: Density Functional Theory of Capillary Condensation in Nanopores. *J. Phys.: Condens. Matter* **2003**, *15*, 347−365.

(49) Olivier, J. P.; Conklin, W. B.; Szombathely, M. V. Determination of Pore Size Distribution from Density Functional Theory: A Comparison of Nitrogen and Argon Results. *Stud. Surf. Sci. Catal.* **1994**, *87*, 81−89.

(50) Gor, G. Y.; Thommes, M.; Cychosz, K. A.; Neimark, A. V. Quenched Solid Density Functional Theory Method for Characterization of Mesoporous Carbons by Nitrogen Adsorption. *Carbon* **2012**, *50*, 1583−1590.

(51) Mandelbrot, B. B.; Blumen, A. Fractal Geometry: What Is It, and What Does It Do? [And Discussion]. *Proc. Roy. Soc. Lond. Math. Phys. Sci.* **1989**, *423*, 3−16.

(52) Pfeifer, P.; Wu, Y. J.; Cole, M. W.; Krim, J. Multilayer Adsorption on a Fractally Rough Surface. *Phys. Rev. Lett.* **1989**, *62*, 1997−2000.

(53) Pyun, S., II.; Rhee, C. An Investigation of Fractal Characteristics of Mesoporous Carbon Electrodes with Various Pore Structures. *Electrochim. Acta* **2004**, *49*, 4171−4180.

(54) Qi, H.; Ma, J.; Wong, P. Adsorption Isotherms of Fractal Surfaces. *Colloids Surf., A* **2002**, *206*, 401−407.

(55) Yao, Y.; Liu, D.; Tang, D.; Tang, S.; Huang, W. Fractal Characterization of Adsorption-Pores of Coals from North China: An Investigation on CH_4 Adsorption Capacity of Coals. *Int. J. Coal Geol.* **2008**, *73*, 27−42.

(56) Pfeifer, P.; Avnir, D. Erratum: Chemistry in noninteger dimensions between two and three. I. Fractal theory of heterogeneous surfaces. *J. Chem. Phys.* **1984**, *80*, 4573.

(57) Wang, Z.; Cheng, Y.; Zhang, K.; Hao, C.; Wang, L.; Li, W.; Hu, B. Characteristics of Microscopic Pore Structure and Fractal Dimension of Bituminous Coal by Cyclic Gas Adsorption/Desorption: An Experimental Study. *Fuel* **2018**, *232*, 495−505.

(58) Jiang, J.; Yang, W.; Cheng, Y.; Zhao, K.; Zheng, S. Pore Structure Characterization of Coal Particles via MIP, N_2 and CO_2 Adsorption: Effect of Coalification on Nanopore Evolution. *Powder Technol.* **2019**, *354*, 136−148.

(59) Mishra, S.; Mendhe, V. A.; Varma, A. K.; Kamble, A. D.; Sharma, S.; Bannerjee, M.; Kalpana, M. S. Influence of Organic and Inorganic Content on Fractal Dimensions of Barakar and Barren Measures Shale Gas Reservoirs of Raniganj Basin, India. *J. Nat. Gas Sci. Eng.* **2018**, *49*, 393−409.

(60) Wang, M.; Xue, H.; Tian, S.; Wilkins, R. W. T.; Wang, Z. Fractal Characteristics of Upper Cretaceous Lacustrine Shale from the Songliao Basin, NE China. *Mar. Pet. Geol.* **2015**, *67*, 144−153.

(61) Liu, X.; Xiong, J.; Liang, L. Investigation of Pore Structure and Fractal Characteristics of Organic-Rich Yanchang Formation Shale in Central China by Nitrogen Adsorption/Desorption Analysis. *J. Nat. Gas Sci. Eng.* **2015**, *22*, 62−72.

(62) Rezaeyan, A.; Pipich, V.; Busch, A. MATSAS: A Small-Angle Scattering Computing Tool for Porous Systems. *J. Appl. Crystallogr.* **2021**, *54*, 697−706.

(63) Loucks, R. G.; Reed, R. M.; Ruppel, S. C.; Hammes, U. Spectrum of Pore Types and Networks in Mudrocks and a Descriptive Classification for Matrix-Related Mudrock Pores. *Am. Assoc. Pet. Geol. Bull.* **2012**, *96*, 1071−1098.

(64) Rabbani, A.; Salehi, S. Dynamic modeling of the formation damage and mud cake deposition using filtration theories coupled with SEM image processing. *J. Nat. Gas Sci. Eng.* **2017**, *42*, 157−168.

(65) Ezeakacha, C. P.; Rabbani, A.; Salehi, S.; Ghalambor, A.. In *Integrated Image Processing and Computational Techniques to Characterize Formation Damage*, 2018; Vol. 2. http://onepetro.org/SPEFD/proceedings-pdf/18FD/1-18FD/D012S007R004/1206119/spe-189509-ms.pdf/1.

(66) Otsu, N. A Threshold Selection Method from Gray-Level Histograms. *IEEE Trans. Syst. Man Cybern.* **1979**, *9*, 62−66.

(67) Rabbani, A.; Jamshidi, S.; Salehi, S. An Automated Simple Algorithm for Realistic Pore Network Extraction from Micro-Tomography Images. *J. Pet. Sci. Eng.* **2014**, *123*, 164−171.

(68) Rabbani, A.; Ayatollahi, S.; Kharrat, R.; Dashti, N. Estimation of 3-D Pore Network Coordination Number of Rocks from Watershed Segmentation of a Single 2-D Image. *Adv. Water Resour.* **2016**, *94*, 264−277.

(69) Smart, S.; Liu, S.; Serra, J. M.; Diniz da Costa, J. C.; Iulianelli, A.; Basile, A. Porous Ceramic Membranes for Membrane Reactors. *Handbook of Membrane Reactors*, 2013, Vol. *1*, pp 298−336. DOI: 10.1533/9780857097330.2.298.

(70) Radlinski, A. P.; Ioannidis, M. A.; Hinde, A. L.; Hainbuchner, M.; Baron, M.; Rauch, H.; Kline, S. R. Angstrom-to-Millimeter Characterization of Sedimentary Rock Microstructure. *J. Colloid Interface Sci.* **2004**, *274*, 607−612.

(71) Rezaeyan, A.; Seemann, T.; Bertier, P.; Pipich, V.; Leu, L.; Kampman, N.; Feoktystov, A.; Barnsley, L.; Busch, A. Understanding Pore Structure of Mudrocks and Pore-Size Dependent Sorption Mechanism Using Small Angle Neutron Scattering. In *SPE/AAPG/SEG Asia Pacific Unconventional Resources Technology Conference 2019*; APUR, 2019, 2019. DOI: 10.15530/AP-URTEC-2019-198285.